

Strip R-CNN: Large Strip Convolution for Remote Sensing Object Detection

Xinbin Yuan¹ Zhaohui Zheng¹ Yuxuan Li¹ Xialei Liu¹ Li Liu³ Xiang Li^{1,2}
 Qibin Hou^{1,2*} Ming-Ming Cheng^{1,2}

¹VCIP, School of Computer Science, NKU ²NKIARI, Futian, Shenzhen ³NUTD
 yxb@mail.nankai.edu.cn, {houqb, cmm}@nankai.edu.cn

Abstract

While witnessed with rapid development, remote sensing object detection remains challenging for detecting high aspect ratio objects. This paper shows that large strip convolutions are good feature representation learners for remote sensing object detection and can detect objects of various aspect ratios well. Based on large strip convolutions, we build a new network architecture called Strip R-CNN, which is simple, efficient, and powerful. Unlike recent remote sensing object detectors that leverage large-kernel convolutions with square shapes, our Strip R-CNN takes advantage of sequential orthogonal large strip convolutions to capture spatial information. In addition, we enhance the localization capability of remote-sensing object detectors by decoupling the detection heads and equipping the localization head with strip convolutions to better localize the target objects. Extensive experiments on several benchmarks, for example DOTA, FAIR1M, HRSC2016, and DIOR, show that our Strip R-CNN can greatly improve previous work. In particular, our 30M model achieves 82.75% mAP on DOTA-v1.0, setting a new state-of-the-art record. Code is available at <https://github.com/YXB-NKU/Strip-R-CNN>.

1. Introduction

Remote sensing object detection has gained significant attention in recent years due to its application in aerial images captured by drones and satellites [32, 33, 36, 42, 45, 58, 79]. A popular detection pipeline is built based on rotated bounding boxes to cover objects of interest. Due to boundary discontinuity and square-like problems [68, 72, 73] and the urgent need to capture long-range information [1, 34], many research breakthroughs have been made to develop

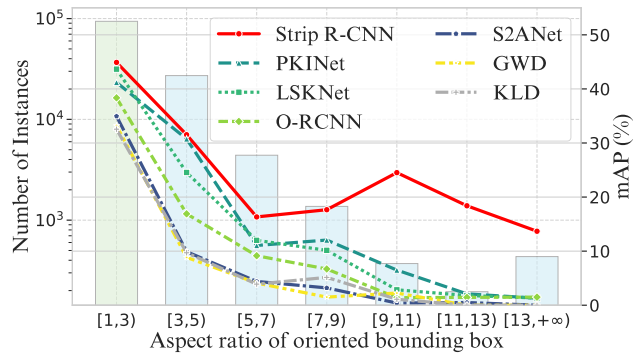


Figure 1. Statistics of the DOTA dataset [63] and the detection performance of several recent state-of-the-art detectors. We can see that slender objects (aspect ratio > 3) occupy a non-negligible proportion and detection performance of previous state-of-the-art models declines as aspect ratio increases.

stronger rotated object detectors, including object representations [31, 64, 65, 67], IoU-simulated loss functions [68, 72–74], and foundation models [1, 34, 52], etc.

Despite the great progress made by previous work, successfully detecting high aspect ratio objects, which are prevalent in remote sensing object detection, is still a challenging problem. To demonstrate this, in Fig. 1, we calculate the statistics of the widely used DOTA dataset [63], which shows that slender objects are quite common in remote sensing scenarios and usually occupy a large proportion of the data. We also experimentally found that existing object detection methods [1, 21, 34, 65, 72, 73] often struggle with slender objects, where detection performance decreases as the aspect ratio of objects increases.

We argue that the difficulties in detecting these objects arise from two primary challenges. First, *high aspect ratio objects contain rich feature information along one spatial dimension, while exhibiting relatively sparse feature in the other*. Traditional detectors based on convolutional neural networks mostly extract input feature maps within square

*Corresponding author.

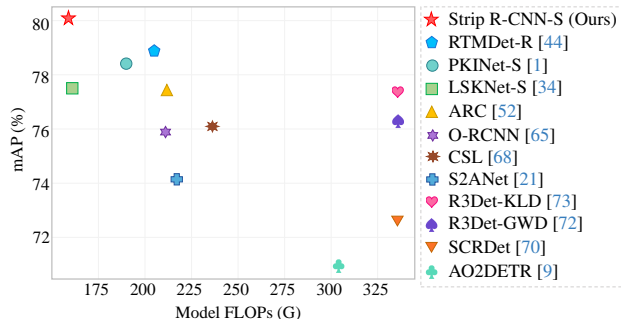


Figure 2. A comprehensive comparison of detection performance on the DOTA dataset of various remote sensing object detectors.

windows. This design greatly restricts their ability to effectively capture the anisotropic context, which can be commonly found in remote sensing images, leading to the inclusion of irrelevant information from surrounding areas. Second, *high aspect ratio objects pose considerable challenges in regression tasks due to their unique geometric properties.* In remote sensing object detection, unlike general object detection, an additional angle regression is required. For high aspect ratio objects, even a small error in angle estimation can lead to significant deviations from the ground truth.

To date, there are few works considering how to deal with challenging high aspect ratio objects. A generic approach widely used in previous methods is to enlarge the receptive field of models with large-kernel convolutions [3, 12, 13, 38]. A typical example should be LSKNet [34], which introduces large-kernel convolutions with a spatial selection mechanism to capture long-range contextual information. PKINet [1] further extends LSKNet and presents a multi-branch structure to enhance the detection ability for large variation of object scales. However, the parallel paradigm of leveraging multiple large-kernel convolutions exacerbates the computational burden, and the complicated block design further restricts the model efficiency. Regarding the high variation of the object aspect ratio, how to efficiently make use of large-kernel convolutions is still an open question.

In this paper, we propose Strip R-CNN, which can efficiently combine the advantage of the square convolution and the strip convolution with less feature redundancy. Our design principles are two-fold. First, the new network architecture should be simple and efficient. Second, it should be good at handling objects of different aspect ratios even when they are high. Given the characteristics of the objects in remote sensing images, we propose using orthogonal large strip convolutions as the main spatial filters, which comprise the core component of our Strip R-CNN, called strip module. As such, our network is quite simple but can generalize well to even objects of especially high aspect ratios as shown in Fig. 1. Furthermore, to conquer the sec-

ond challenge mentioned above, we decouple the detection heads used in previous remote sensing object detections and strengthen the localization branch with the proposed strip module. We found that this can not only assist in improving the localization capability of our method but also help more accurately regress the box angles.

To our knowledge, Strip R-CNN is the first work to explore how to take advantage of large strip convolutions for remote sensing object detection. Despite simplicity and the lightweight nature, our Strip R-CNN achieves state-of-the-art performance on the standard DOTA benchmark without bells and whistles, as shown in Fig. 2. Notably, our model Strip R-CNN-S with only 30M learnable parameters achieves the best results on DOTA leaderboard with 82.75% mAP. We also conduct extensive experiments on several other remote sensing datasets, including FAIR1M, HRSC2016, and DIOR, and show the superiority of our Strip R-CNN over other methods. We hope that our design principles could provide new research insights for the remote sensing imagery community.

2. Related Work

Remote Sensing Object Detection. Generic object detection typically relies on horizontal bounding boxes to detect objects [5, 54, 81]. However, in remote sensing scenarios, where objects are arbitrarily oriented, horizontal boxes often fail to precisely localize objects and tend to include background information or other objects [63]. Therefore, rotated bounding boxes are generally adopted for object representation. Early representations of rotated bounding boxes use five parameters (x, y, w, h, θ) [11, 40, 70]. However, due to the periodicity of the angle, training models based on this representation often face boundary discontinuity problems in regression [68, 72, 74]. To address this issue, several approaches propose improved representations [16, 31, 60, 64, 65, 67, 71, 75] for rotated bounding boxes. For instance, Oriented R-CNN [65] replaces the angle with midpoint offsets, leading to a six-parameter representation $(x, y, w, h, \Delta\alpha, \Delta\beta)$, which significantly enhances detector performance. COBB [64] introduces a continuous representation of rotated boxes with nine parameters based on the aspect ratio of the minimum enclosing rectangle to the rotated bounding box areas. There are also approaches focusing on mitigating the discontinuity problem in boundary regression through loss functions [8, 26, 53, 72, 73]. For example, GWD [72] and KLD [73] convert rotated bounding boxes into 2D Gaussian distributions and use Gaussian Wasserstein Distance and Kullback-Leibler Divergence as the loss functions. KFIOU [74] employs Gaussian modeling and Kalman filtering to propose the approximate SKewIoU Loss.

Despite the great progress made by previous work, suc-

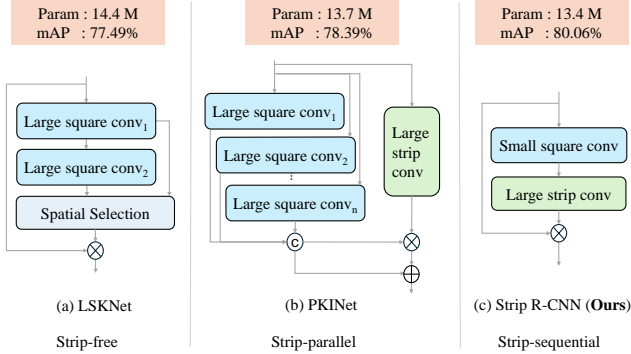


Figure 3. Structural comparison between our proposed strip module and other representative methods using large-kernel convolutions, including LSKNet [34] and PKINet [1].

successfully detecting high aspect ratio objects, which are prevalent in remote sensing object detection, is still a challenging problem. Our method carefully considers the difficulties posed by these objects and take advantage of large strip convolutions to make our network generalize well to the challenging slender objects, which to our knowledge has not been explored before in this research field.

Large Kernel Networks for Remote Sensing Object Detection. Convolution with large kernel has been an emerging and promising solution to remote sensing object detection, which has been validated to have highly competitive performance against the Transformer-based methods in image classification and segmentation [3, 12, 13, 18, 19, 27, 28, 38, 76]. In remote sensing object detection, some approaches put efforts on employing large-kernel convolutions to get long-range contextual information [1, 35]. For example, LSKNet [35] utilizes large kernel convolutions and a selection mechanism to model the contextual information needed for different object categories. PKINet [1] arranges multiple large-kernel convolutions in parallel to extract dense texture features across diverse receptive fields, and introduces a context anchor attention mechanism to capture relationships between distant pixels. However, the parallel paradigm of leveraging multiple large-kernel convolutions exacerbates the computational burden, and the complicated block design makes the model not efficient. Regarding the high variation of the object aspect ratio, how to efficiently make use of large-kernel convolutions is still an open question. To our knowledge, Strip R-CNN is the first work to explore how to take advantage of large strip convolutions for remote sensing object detection.

3. Strip R-CNN

In this section, we describe the architecture of the proposed Strip R-CNN in detail. Our goal is to advance remote sensing object detectors with large strip convolutions so that the

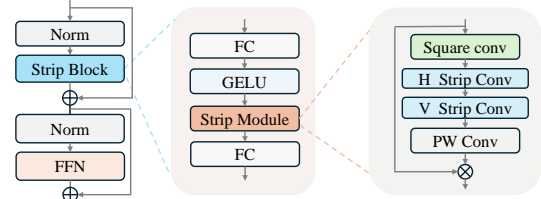


Figure 4. Structure of our basic block.

Table 1. Variants of StripNet backbone. C_i : feature channel number; D_i : number of strip blocks in each stage i .

Model	$\{C_1, C_2, C_3, C_4\}$	$\{D_1, D_2, D_3, D_4\}$	#P	FLOPs
* StripNet-T	{32, 64, 160, 256}	{3, 3, 5, 2}	3.8M	18.2G
* StripNet-S	{64, 128, 320, 512}	{2, 2, 4, 2}	13.3M	52.3G

resulting model can perform well on objects of different aspect ratios. This is different from previous work that emphasizes the importance of convolutions with large square kernels, as shown in Fig. 3.

3.1. Overall Architecture

Based on the O-RCNN framework [65], our Strip R-CNN replace the backbone and detection head with our StripNet backbone and strip head, respectively. Specifically, the backbone is mainly composed of basic blocks proposed as illustrated in Fig. 4, which consists of two residual sub-blocks: the strip sub-block and the feed-forward network sub-block. The strip sub-block is built upon a small-kernel standard convolution and two convolutions with large strip-shaped kernels to capture robust features for objects of different aspect ratios. For the feed-forward network sub-block, we simply follow LSKNet [34], which is used to facilitate channel mixing and feature refinement. The detailed configurations of different variants of our StripNet backbone are shown in Tab. 1. For the stem layers, we keep them the same to LSKNet [34]. For the detection head, we decouple the localization branch from the original O-RCNN head and enhance it with the proposed strip module, resulting in our strip head, which will be presented in Sec. 3.3.

3.2. Strip Module

As discussed in Sec. 1, large square kernel convolutions provide essential long-range contextual information for remote sensing applications, but may include irrelevant features from the background regions. PKINet involves strip convolutions in model design [1] while it still relies on parallel large square kernel convolutions, which introduces computational burdens and feature redundancy. Our objective is to efficiently extract essential features for objects of varying aspect ratios. The outcome is a sequential paradigm that efficiently combines the advantages of both standard and strip convolutions without requiring additional information fusion module. In what follows, we provide a detailed

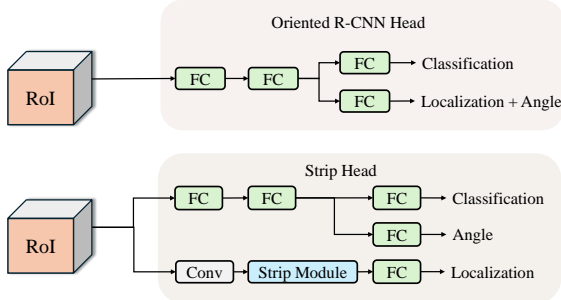


Figure 5. Structural comparison of Oriented R-CNN head and strip head. In our strip head, the classification and angle prediction heads share two fully connected layer, while the localization head incorporates our strip module.

description of the core of our basic block: strip module.

Given an input tensor $\mathbf{X} \in \mathbb{R}^{C \times H \times W}$ with C channels, a depthwise convolution with square kernels $\mathbf{K} \in \mathbb{R}^{C \times k_H \times k_W}$ is first applied to extract local contextual features, yielding \mathbf{Z} , where $H \times W$ and $k_H \times k_W$ are the feature size and kernel size, respectively. In practical use, we set $k_H \times k_W$ to 5×5 . After the initial depthwise convolution, we use two sequential depthwise convolution of large strip-shaped kernels to better capture objects of high aspect ratios. The output is denoted as $\hat{\mathbf{Z}}$. Unlike standard convolutions that extract features from a square region for each time, large strip convolutions allow the network to focus more on features along either the horizontal or the vertical axis. The combined use of horizontal and vertical large strip convolutions enables the network to collect directional features across both spatial axes, enhancing the representations of elongated or narrow structures in spatial dimension.

To further enhance the interaction of the features across the channel dimension, a simple point-wise convolution is applied to transform $\hat{\mathbf{Z}}$ to \mathbf{Y} . In this way, each position of the resulting feature map \mathbf{Y} encodes both horizontal and vertical features across a wide spatial area. Finally, following [19, 28], we regard the feature map \mathbf{Y} as attention weights to reweigh the input X , which can be formulated as

$$\hat{\mathbf{Y}} = \mathbf{X} \cdot \mathbf{Y}, \quad (1)$$

where ‘ \cdot ’ denotes the element-wise multiplication operation. Fig. 4 provides a diagrammatic illustration of the proposed strip module. In our experiments, we will discuss how to choose the kernel size of the strip convolutions.

It is important to emphasize that Strip R-CNN is much simpler than previous remote sensing object detectors using large-kernel convolutions as shown in Fig. 3. We do not utilize any spatial or channel attention mechanisms in our basic block design nor compound fusion operations with different types of large-kernel convolutions. This makes our Strip R-CNN quite simple but has great performance on different remote sensing detection benchmarks. Moreover, we

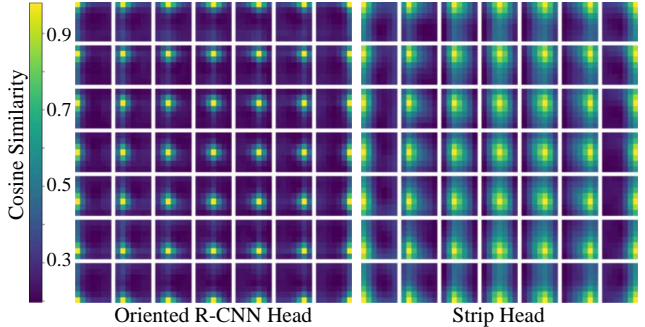


Figure 6. Spatial correlation map comparison of the Oriented R-CNN head and our strip head. Our strip head has significantly more spatial correlations in the output feature maps.

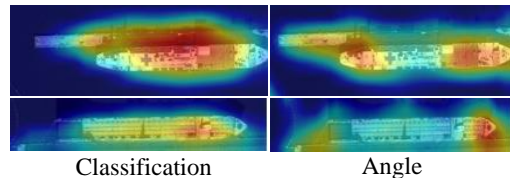


Figure 7. Spatial sensitivity heatmap comparison for classification and angle prediction in the output feature maps.

found that there is no significant difference in applying horizontal strip convolutions before vertical ones or vice versa. Both approaches are effective.

3.3. Detection Head with Strip Convolutions

In localization tasks, models should be sensitive to transformations, as the accuracy of localization depends on the positions of input objects. Previous strong remote sensing object detectors [1, 34] adopt the popular Oriented R-CNN framework [65], whose detection head shares the same fully connected layers for classification and localization tasks, as shown in Fig. 5. However, fully connected layers have limited spatial correlation as demonstrated in [62], making them transformation-insensitive and unsuitable for precise localization.

A better solution might be to decouple the classification and localization tasks and using small kernel convolutions in the localization branch as suggested in [62]. However, our analysis of spatial correlation maps shows that small kernel convolutions capture only short-range spatial correlations, as illustrated on the left of Fig. 6. These short-range correlations are inadequate for accurately localizing slender objects, which require long-range dependencies. To effectively localize objects of varying aspect ratios, we argue that the localization head should be able to capture long-range dependencies, similar to those handled by the backbone network. Large strip convolutions, which capture both horizontal and vertical features across a broad spatial area, provide the extended spatial correlations necessary for better localization. Therefore, we propose using large strip convo-

lutions in the localization branch to enhance the detector’s localization capabilities.

Furthermore, predicting the parameters x , y , w , h , and θ together may lead to the issue of coupled features [77]. To address this, we decouple the prediction of θ from the other parameters (x , y , w , h). Building on this decoupling approach, we investigate the spatial sensitivity regions of the classification and angle predictions in the output feature maps. The spatial sensitivity heat map is shown in Fig. 7, where the first column represents the classification sensitivity, and the second shows the angle sensitivity. Our observation reveals that the spatial sensitivity for classification is concentrated in the central areas of the objects, while the sensitivity for angle is primarily focused near the object borders. The sensitive regions for classification and angle predictions share some overlap and exhibit some complementary characteristics. Based on this, we propose the use of shared fully connected layers for both classification and angle predictions. The structure of the strip head is shown at the bottom of Fig. 5. Detailed configurations are described below.

Classification head: The classification head simply utilizes two fully connected layers with an output dimension of 1024. Using fully connected layers in the classification head has been shown to be a good choice, as demonstrated in Double-Head RCNN [62], so we keep it unchanged.

Localization head: The localization head begins with a standard 3×3 convolution to extract local features. Then we add a strip module, followed by a fully connected layer to collect long-range spatial dependencies.

Angle head: For angle prediction, we adopt three fully connected layers to effectively estimate angular information, which we found works well. Note that the first two fully connected layers share parameters with the classification head.

Loss function: All three heads, including classification head, localization head, and angle estimation head, are jointly trained end-to-end. The overall loss function can be written as follows:

$$\mathcal{L} = \mathcal{L}_c + \mathcal{L}_l + \mathcal{L}_a, \quad (2)$$

where \mathcal{L}_c is cross entropy loss for classification head, \mathcal{L}_l , and \mathcal{L}_a are the Smooth L1 loss [17] for localization head and angle head, respectively.

It is worth noting that our detection head incorporates tce is cross entropy loss, proposed strip module. This design largely improves the detection capability compared to the original Oriented R-CNN head. As shown in Fig. 6, from the visualization of the spatial sensitivity of different methods, we can see that the Oriented R-CNN head has a similar spatial correlation pattern on the output feature maps. However, our strip head has much more spatial correlations in

the output feature maps. We will show that this enables our method to be able to better localize objects even of higher aspect ratios.

4. Experiments

4.1. Datasets

We conduct extensive experiments on five popular remote sensing object detection datasets.

- **DOTA-v1.0** [63] is a large-scale dataset for remote sensing detection which contains 2,806 images, 188,282 instances, and 15 categories.
- **DOTA-v1.5** [63] is a more challenging dataset which contains 403,318 instances and 16 categories.
- **FAIR1M-v1.0** [57] is a remote sensing dataset that consists of 15,266 images, 1 million instances, and 37 categories.
- **HRSC2016** [39] is a remote sensing dataset that contains 1061 aerial images and 2,976 instances.
- **DIOR-R** [6] contains 23,463 images and 192,518 instances.

4.2. Implementation Details

Our training process is divided into two stages: pretraining on ImageNet [10] followed by fine-tuning on downstream remote sensing datasets. In the ablation experiments, we consistently train all the models for 100 epochs. To achieve higher performance, we train the models for 300 epochs in the final results table. The number of training epochs for the DOTA, DOTA-v1.5, HRSC2016, FAIR1M-v1.0, and DIOR-R datasets are set to 12, 12, 36, 12, and 12, respectively, following previous methods. The learning rates are set to 0.0001, 0.0001, 0.0004, 0.0001, and 0.0001, respectively. The input sizes for the HRSC2016 and DIOR-R datasets are 800×800 , while for the DOTA-v1.0, DOTA-v1.5 and FAIR1M-v1.0 datasets, the input sizes are 1024×1024 . During training, we employ the AdamW [43] optimizer with $\beta_1 = 0.9$, $\beta_2 = 0.999$, and a weight decay of 0.05. All the models are trained on 8 NVIDIA 3090 GPUs with a batch size of 8, and test is conducted on a single NVIDIA 3090 GPU.

4.3. Main Results

We first compare our Strip R-CNN with recent state-of-the-art methods with strong backbones implemented within the Oriented R-CNN [65] framework on the DOTA v1.0 dataset. As shown in Tab. 2, Strip R-CNN-S achieves an improvement of 1.67% while using 0.4% fewer parameters and only 74.3% of the computations required by PKINet-S [1]. Additionally, Strip R-CNN-S shows a 2.57% enhancement over LSKNet-S [34] utilizing 1.1% fewer parameters and 2.2% less computations.

Table 2. Comparisons with different backbone models on the DOTA-v1.0 dataset. Params and FLOPs are computed for backbone only. All backbones are pretrained on ImageNet for 300 epochs. Our StripNet-S achieves higher mAP than previous popular backbones.

Model (Backbone)	#P↓	FLOPs↓	FPS	mAP (%)
ResNet-50 [23]	23.3M	86.1G	21.8	75.87
LSKNet-S [34]	14.4M	54.4G	20.7	77.49
PKINet-S [1]	13.7M	70.2G	12.0	78.39
*StripNet-S	13.3M	52.3G	17.7	80.06

Results on DOTA-v1.0 [63]. We conduct a comparative analysis of different models and present detailed results for mean Average Precision (mAP) and Average Precision (AP) across categories on the DOTA dataset. As shown in Tab. 3, our single-scale evaluation demonstrates a 1.67% improvement over PKINet-S. Furthermore, with multi-scale training and testing, we achieve 82.28% mAP for a single model. By ensembling the results of RTMDet and Strip R-CNN, following the model ensemble strategy in MoCAE [50], we further achieve 82.75% mAP, setting a new state-of-the-art record.

Results on DOTA-v1.5 [63]. In this dataset with minuscule instances, as shown in Tab. 4, our approach achieves outstanding performance, demonstrating its efficacy and generalization ability to small objects. Our Strip R-CNN outperforms the former state-of-the-art method, achieving an improvement of 0.8%.

Results on FAIR1M-v1.0 [57]. The results in Tab. 5 reveal that our Strip R-CNN reaches a highly competitive mAP score of 48.26%. Our method could improve 0.39% mAP for LSKNet [34] and surpassing all other methods by a significant margin.

Results on DIOR-R [6]. As shown in Tab. 7, we observe 2.80% improvement over LSKNet [34] and 1.67% improvement over PKINet [1].

Results on HRSC2016 [39]. We achieve 98.70% mAP under the VOC2012 [15] metric, which is the state-of-the-art performance with 0.16% mAP improvement over PKINet [1] and 0.24% mAP over LSKNet [34]. The results are shown in Tab. 6.

Across multiple datasets, our method consistently surpasses previous state-of-the-art approaches, demonstrating its generalizability and effectiveness.

4.4. Ablation Studies

Kernel size of strip convolutions. The kernel size in strip convolutions is critical for our proposed strip module. We experiment with large kernel sizes, starting from 11 and increasing in increments of 4. Smaller kernels are ineffective in capturing features of high aspect ratio objects, while a

kernel size of 15 yielded satisfactory results, with further improvement observed at 19. We also test various kernel sizes at different network stages, exploring both increasing and decreasing strategies. Larger kernels in shallow layers combined with smaller kernels in deeper layers produce good results. In contrast, using smaller kernels in the shallow layers leads to significant performance drops, indicating that shallow layers benefit from larger receptive fields. Consequently, we select 19 as the optimal kernel size for the strip module at all stages.

Ablation on strip module design We conduct ablation experiments to analyze the design choices in the strip module. First, we assess the role of depth-wise square convolution. Removing this component leads to a significant performance drop, emphasizing the importance of square convolution for capturing features of square-shaped objects. Next, we examine the integration of horizontal and vertical large strip convolutions, comparing parallel and sequential arrangements. The sequential configuration outperforms the parallel one, as the latter lacks effective two-dimensional modeling, merely combining the two strip convolutions without capturing the overall object structure. Furthermore, substituting the sequential large strip convolutions with either a 19×19 large kernel convolution or a 7×7 dilated convolution with a dilation rate of 3 results in noticeable performance loss, further validating the effectiveness of the large strip convolutions. The results are reported in Tab. 9.

Ablation on strip head design. In designing the strip head, we initially decouple the head into (x, y) , (w, h) , and θ branches, applying the strip module to either the (x, y) or (w, h) branches. This approach shows moderate improvement. Combining the (x, y) and (w, h) branches yields slightly better results, probably due to the complementary and similar features shared by object position and shape information. For the θ branch, we found that fully connected layers slightly outperform convolutional layers. Therefore, we adopt two fully connected layers for the θ branch, and share them with the classification branch in that the sensitive regions for classification and angle predictions share some overlap and exhibit some complementary characteristics, as discussed in Sec. 3.3. Simply applying the strip module to the localization branch produces noticeable improvements. We argue that more specialized structures tailored to different regression parameters could further enhance performance. Results are shown in Tab. 10.

The effectiveness of the strip head. As can be seen in Tab. 11, we compare the performance of two different detectors before and after incorporating the strip head. The results demonstrate that our strip head consistently improves the performance of other detectors, confirming its effectiveness and generalizability. For the ROI Transformer, our method achieves a significant improvement of 5.0 mAP,

Table 3. Comparisons with SOTA methods on the DOTA-v1.0 dataset with single-scale and multi-scale training and testing. The StripNet-S backbone is pretrained on ImageNet for 300 epochs. †: Model ensemble as in MoCAE [50].

Method	Pre.	mAP ↑	#P ↓	FLOPs ↓	PL	BD	BR	GTF	SV	LV	SH	TC	BC	ST	SBF	RA	HA	SP	HC
<i>Single-Scale</i>																			
EMO2-DETR [29]	IN	70.91	74.3M	304G	87.99	79.46	45.74	66.64	78.90	73.90	73.30	90.40	80.55	85.89	55.19	63.62	51.83	70.15	60.04
CenterMap [61]	IN	71.59	41.1M	198G	89.02	80.56	49.41	61.98	77.99	74.19	83.74	89.44	78.01	83.52	47.64	65.93	63.68	67.07	61.59
AO2-DETR [9]	IN	72.15	74.3M	304G	86.01	75.92	46.02	66.65	79.70	79.93	89.17	90.44	81.19	76.00	56.91	62.45	64.22	65.80	58.96
SCRDet [70]	IN	72.61	41.9M	-	89.98	80.65	52.09	68.36	68.36	60.32	72.41	90.85	87.94	86.86	65.02	66.68	66.25	68.24	65.21
R3Det [69]	IN	73.70	41.9M	336G	89.5	81.2	50.5	66.1	70.9	78.7	78.2	90.8	85.3	84.2	61.8	63.8	68.2	69.8	67.2
Rol Trans. [11]	IN	74.05	55.1M	200G	89.01	77.48	51.64	72.07	74.43	77.55	87.76	90.81	79.71	85.27	58.36	64.11	76.50	71.99	54.06
S ² ANet [21]	IN	74.12	38.5M	-	89.11	82.84	48.37	71.11	78.11	78.39	87.25	90.83	84.90	85.64	60.36	62.60	65.26	69.13	57.94
SASM [25]	IN	74.92	36.6M	-	86.42	78.97	52.47	69.84	77.30	75.99	86.72	90.89	82.63	85.66	60.13	68.25	73.98	72.22	62.37
G.V. [67]	IN	75.02	41.1M	198G	89.64	85.00	52.26	77.34	73.01	73.14	86.82	90.74	79.02	86.81	59.55	70.91	72.94	70.86	57.32
O-RCNN [65]	IN	75.87	41.1M	199G	89.46	82.12	54.78	70.86	78.93	83.00	88.20	90.90	87.50	84.68	63.97	67.69	74.94	68.84	52.28
ReDet [22]	IN	76.25	31.6M	-	88.79	82.64	53.97	74.00	78.13	84.06	88.04	90.89	87.78	85.75	61.76	60.39	75.96	68.07	63.59
R3Det-GWD [72]	IN	76.34	41.9M	336G	88.82	82.94	55.63	72.75	78.52	83.10	87.46	90.21	86.36	85.44	64.70	61.41	73.46	76.94	57.38
COBB [64]	IN	76.52	41.9M	-	-	-	-	-	-	-	-	-	-	-	-	-	-	-	-
R3Det-KLD [73]	IN	77.36	41.9M	336G	88.90	84.17	55.80	69.35	78.72	84.08	87.00	89.75	84.32	85.73	64.74	61.80	76.62	78.49	70.89
ARC [74]	IN	77.35	74.4M	217G	89.40	82.48	55.33	73.88	79.37	84.05	88.06	90.90	86.44	84.83	63.63	70.32	74.29	71.91	65.43
LSKNet-S [34]	IN	77.49	31.0M	161G	89.66	85.52	57.72	75.70	74.95	78.69	88.24	90.88	86.79	86.38	66.92	63.77	77.77	74.47	64.82
PSC [78]	IN	78.10	-	-	-	-	-	-	-	-	-	-	-	-	-	-	-	-	-
PKINet-S [1]	IN	78.39	30.8M	190G	89.72	84.20	55.81	77.63	80.25	84.45	88.12	90.88	87.57	86.07	66.86	70.23	77.47	73.62	62.94
RTMDet-R [44]	IN	78.85	52.3M	205G	89.43	84.21	55.20	75.06	80.81	84.53	88.97	90.90	87.38	87.25	63.09	67.87	78.09	80.78	69.13
★ Strip R-CNN-S	IN	80.06	30.5M	159G	88.91	86.38	57.44	76.37	79.73	84.38	88.25	90.86	86.71	87.45	69.89	66.82	79.25	82.91	75.58
<i>Multi-Scale</i>																			
CSL [68]	IN	76.17	37.4M	236G	90.25	85.53	54.64	75.31	70.44	73.51	77.62	90.84	86.15	86.69	69.60	68.04	73.83	71.10	68.93
CFA [20]	IN	76.67	-	-	89.08	83.20	54.37	66.87	81.23	80.96	87.17	90.21	84.32	86.09	52.34	69.94	75.52	80.76	67.96
DAFNet [30]	IN	76.95	-	-	89.40	86.27	53.70	60.51	82.04	81.17	88.66	90.37	83.81	87.27	53.93	69.38	75.61	81.26	70.86
DODet [7]	IN	80.62	-	-	89.96	85.52	58.01	81.22	78.71	85.46	88.59	90.89	87.12	87.80	70.50	71.54	82.06	77.43	74.47
AOPG [6]	IN	80.66	-	-	89.88	85.57	60.90	81.51	78.70	85.29	88.85	90.89	87.60	87.65	71.66	68.69	82.31	77.32	73.10
KFloU [74]	IN	80.93	58.8M	206G	89.44	84.41	62.22	82.51	80.10	86.07	88.68	90.90	87.32	88.38	72.80	71.95	78.96	74.95	75.27
RTMDet-R [44]	CO	81.33	52.3M	205G	88.01	86.17	58.54	82.44	81.30	84.82	88.71	90.89	88.77	87.37	71.96	71.18	81.23	81.40	77.13
RVSA [59]	MA	81.24	114.4M	414G	88.97	85.76	61.46	81.27	79.98	85.31	88.30	90.84	85.06	87.50	66.77	73.11	84.75	81.88	77.58
LSKNet-S [34]	IN	81.64	31.0M	161G	89.57	86.34	63.13	83.67	82.20	86.10	88.66	90.89	88.41	87.42	71.72	69.58	78.88	81.77	76.52
★ Strip R-CNN-T	IN	81.40	20.5M	123G	89.14	84.90	61.78	83.50	81.54	85.87	88.64	90.89	88.02	87.31	71.55	70.74	78.66	79.81	78.16
★ Strip R-CNN-S	IN	82.28	30.5M	159G	89.17	85.57	62.40	83.71	81.93	86.58	88.84	90.86	87.97	87.91	72.07	71.88	79.25	82.45	82.82
★ Strip R-CNN-S†	IN	82.75	30.5M	159G	88.99	86.56	61.35	83.94	81.70	85.16	88.57	90.88	88.62	87.36	75.13	74.34	84.58	81.49	82.56

Table 4. Comparisons with SOTA methods on the DOTA-v1.5 dataset with single-scale training and testing. The StripNet-S backbone is pretrained on ImageNet for 300 epochs.

Method	RetinaNet-O [37]	FR-O [54]	Mask RCNN [24]	HTC [4]	ReDet [22]	DCFL [66]	LSKNet-S [34]	PKINet-S [1]	Strip R-CNN-S
mAP (%)	59.16	62.00	62.67	63.40	66.86	67.37	70.26	71.47	72.27

which is a remarkable increase. Similarly, the other detector Rotated Faster R-CNN also receives performance gains, further validating that our approach is compatible with a wide range of detectors and is able to reliably enhance detection performance.

4.5. Visual Analysis

We also present detection results and Eigen-CAM [49] visualizations in Fig. 8. From these images, it is evident that for high aspect ratio objects, previous methods such as Oriented-RCNN and LSKNet exhibit issues like missed detections and significant localization errors. In contrast, our method can successfully detect the high aspect ratio objects.

The Eigen-CAM visualizations also show strong activations of our method for these objects, further validating that our approach can alleviate the challenges associated with detecting high aspect ratio objects.

Additionally, to further substantiate the superiority of our method in detecting high aspect ratio objects, we conduct additional experiments on the DOTA dataset. The models are trained on the DOTA train set and tested on the val set, following the evaluation method used in [82]. We assess detection performance across objects with different aspect ratios. As shown in Fig. 1, the results indicate that within the aspect ratio range of 1-5, our method and previous approaches show comparable performance, with only

Table 5. Comparisons with SOTA methods on the FAIR1M-v1.0 dataset. The StripNet-S backbone is pretrained on ImageNet for 300 epochs. *: Results are referenced from the FAIR1M paper [57].

Method	G. V.* [67]	RetinaNet* [37]	C-RCNN* [2]	F-RCNN* [54]	RoI Trans.* [11]	O-RCNN [65]	LSKNet-S [34]	Strip R-CNN-S
mAP (%)	29.92	30.67	31.18	32.12	35.29	45.60	47.87	48.26

Table 6. Comparisons with SOTA methods on HRSC2016. mAP (07/12): VOC 2007 [14]/2012 [15] metrics. The StripNet-S backbone is pretrained on ImageNet for 300 epochs.

Method	Pre.	mAP(07)↑	mAP(12)↑	#P ↓	FLOPs ↓
DRN [51]	IN	-	92.70	-	-
DAL [46]	IN	89.77	-	36.4M	216G
GWD [72]	IN	89.85	97.37	47.4M	456G
AOPG [6]	IN	90.34	96.22	-	-
O-RCNN [65]	IN	90.50	97.60	41.1M	199G
RTMDet [44]	CO	90.60	97.10	52.3M	205G
LSKNet-S [34]	IN	90.65	98.46	31.0M	161G
PKINet-S [1]	IN	90.65	98.54	30.8M	190G
* Strip R-CNN-S	IN	90.60	98.70	30.5M	159G

Table 7. Comparisons with the SOTA methods on the DIOR-R Datasets. The StripNet-S backbone is pretrained on ImageNet for 300 epochs.

Method	Pre.	#P ↓	FLOPs ↓	mAP (%)
RetinaNet-O [37]	IN	-	-	57.55
Faster RCNN-O [54]	IN	41.1M	198G	59.54
TIOE-Det [48]	IN	41.1M	198G	61.98
O-RCNN [65]	IN	41.1M	199G	64.30
ARS-DETR [80]	IN	41.1M	198G	66.12
O-RepPoints [31]	IN	36.6M	-	66.71
DCFL [66]	IN	-	-	66.80
LSKNet-S [34]	IN	31M	161G	65.90
PKINet-S [1]	IN	30.8M	190G	67.03
* Strip R-CNN-S	IN	30.5M	159G	68.70

Table 8. Ablation study on the kernel size of our proposed strip module at four stages of the StripNet backbone network. We adopt the StripNet-S backbone pretrained on ImageNet for 100 epochs. The best result is obtained when using kernel size 19 at all stages.

Kernel Size	#P↓	FLOPs↓	mAP (%)
(19,19,19,19)	13.30M	52.34G	81.75
(15,15,15,15)	13.28M	52.19G	81.64
(11,11,11,11)	13.26M	52.03G	81.22
(15,17,19,21)	13.31M	52.26G	81.37
(21,19,17,15)	13.29M	52.34G	81.72

minor differences. However, for objects with larger aspect ratios, our method demonstrates an obvious advantage.

5. Conclusions

In this paper, we alleviate the challenge of detecting slender objects in remote sensing scenarios by leveraging large strip convolutions to better extract features and improve localization of such objects. Based on large strip convolutions, we

Table 9. Ablation study on the design of our proposed strip module. We adopt the StripNet-S backbone pretrained on ImageNet for 100 epochs. d: dilation rate.

5 × 5 Square Conv	Large Strip Conv		#P ↓	FLOPs ↓	mAP (%)
	Sequential	Parallel			
✗	✓	✗	13.23M	51.84G	81.38
✓	✓	✗	13.30M	52.34G	81.75
✓	✗	✓	13.33M	52.52G	81.54
✓	19 × 19 Square Conv		14.17M	58.41G	81.44
✓	7 × 7 Square Conv d=3		13.30M	52.34G	81.55

Table 10. Ablation study of the strip head design. fc refers to using two fully connected layers in this branch. $conv$ refers to using two depth-wise 3×3 convolutional layers followed by point-wise convolution in this branch. $strip$ refers to replacing the latter 3×3 convolutional layer with our designed strip module. We adopt the StripNet-S backbone pretrained on ImageNet for 100 epochs.

Different Head Structure	mAP (%)
$(x, y, w, h, \theta)_{fc}$	81.75
$(x, y)_{conv}, (w, h)_{conv}, (\theta)_{fc}$	81.76
$(x, y)_{conv}, (w, h)_{conv}, (\theta)_{conv}$	81.72
$(x, y)_{strip}, (w, h)_{conv}, (\theta)_{fc}$	81.88
$(x, y)_{conv}, (w, h)_{strip}, (\theta)_{fc}$	81.77
$(x, y)_{conv}, (w, h)_{conv}, (\theta)_{strip}$	81.81
$(x, y, w, h)_{strip}, (\theta)_{fc}$	81.96
$(x, y, w, h)_{strip}, (\theta)_{strip}$	81.93

Table 11. Effectiveness of strip head on other remote sensing object detectors.

Method	Head	mAP (%)
Faster RCNN-O [54]	Original Head	76.17
	Strip Head	77.88
RoI Trans. [11]	Original Head	74.61
	Strip Head	79.37

propose the simple yet highly effective Strip R-CNN. Extensive experiments demonstrate that our method exhibits strong generalization capability and achieve state-of-the-art performance on several remote sensing benchmarks. We hope this research could facilitate the development of object detection in the remote sensing field.

References

- [1] Xinhao Cai, Qiuxia Lai, Yuwei Wang, Wenguan Wang, Zeren Sun, and Yazhou Yao. Poly kernel inception network

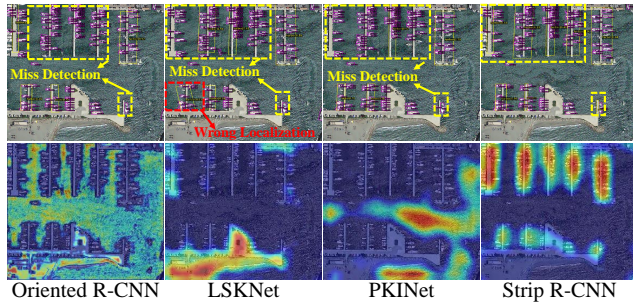


Figure 8. **Top:** Detection results. Our method Strip R-CNN can successfully capture the high aspect ratio objects. **Bottom:** Eigen-CAM visualizations. The Eigen-CAM visualization of our method shows strong activations for high aspect ratio objects, further validating the effectiveness of our approach.

- for remote sensing detection. In *CVPR*, pages 27706–27716, 2024. 1, 2, 3, 4, 5, 6, 7, 8
- [2] Zhaowei Cai and Nuno Vasconcelos. Cascade R-CNN: Delving into high quality object detection. In *CVPR*, 2018. 8, 2
- [3] Honghao Chen, Xiangxiang Chu, Yongjian Ren, Xin Zhao, and Kaiqi Huang. Pelk: Parameter-efficient large kernel convnets with peripheral convolution. In *CVPR*, pages 5557–5567, 2024. 2, 3
- [4] Kai Chen, Jiangmiao Pang, Jiaqi Wang, Yu Xiong, Xiaoxiao Li, Shuyang Sun, Wansen Feng, Ziwei Liu, Jianping Shi, Wanli Ouyang, Chen Change Loy, and Dahua Lin. Hybrid task cascade for instance segmentation. In *CVPR*, 2019. 7, 2
- [5] Yuming Chen, Xinbin Yuan, Ruiqi Wu, Jiabao Wang, Qibin Hou, and Ming-Ming Cheng. YOLO-MS: Rethinking multi-scale representation learning for real-time object detection. *ArXiv*, 2023. 2
- [6] Gong Cheng, Jiabao Wang, Ke Li, Xingxing Xie, Chunbo Lang, Yanqing Yao, and Junwei Han. Anchor-free oriented proposal generator for object detection. *IEEE TGRS*, 60:1–11, 2022. 5, 6, 7, 8, 1
- [7] Gong Cheng, Yanqing Yao, Shengyang Li, Ke Li, Xingxing Xie, Jiabao Wang, Xiwen Yao, and Junwei Han. Dual-aligned oriented detector. *IEEE TGRS*, 2022. 7
- [8] Gong Cheng, Yanqing Yao, Shengyang Li, Ke Li, Xingxing Xie, Jiabao Wang, Xiwen Yao, and Junwei Han. Dual-aligned oriented detector. *IEEE TGRS*, 2022. 2
- [9] Linhui Dai, Hong Liu, Hao Tang, Zhiwei Wu, and Pinhao Song. AO2-DETR: Arbitrary-oriented object detection transformer. *IEEE TCSVT*, 2022. 2, 7
- [10] Jia Deng, Wei Dong, Richard Socher, Li-Jia Li, Kai Li, and Li Fei-Fei. ImageNet: A large-scale hierarchical image database. In *CVPR*, 2009. 5, 4
- [11] Jian Ding, Nan Xue, Yang Long, Gui-Song Xia, and Qikai Lu. Learning RoI transformer for oriented object detection in aerial images. In *CVPR*, 2019. 2, 7, 8, 3, 4
- [12] Xiaohan Ding, Xiangyu Zhang, Jungong Han, and Guiguang Ding. Scaling up your kernels to 31×31: Revisiting large kernel design in CNNs. In *CVPR*, 2022. 2, 3
- [13] Xiaohan Ding, Yiyuan Zhang, Yixiao Ge, Sijie Zhao, Lin Song, Xiangyu Yue, and Ying Shan. Unireplknet: A universal perception large-kernel convnet for audio video point cloud time-series and image recognition. In *CVPR*, pages 5513–5524, 2024. 2, 3
- [14] M. Everingham, L. Van Gool, C. K. I. Williams, J. Winn, and A. Zisserman. The PASCAL Visual Object Classes Challenge 2007 (VOC2007) Results, 2007. 8
- [15] M. Everingham, L. Van Gool, C. K. I. Williams, Winn, and A. Zisserman. The PASCAL Visual Object Classes challenge 2012 (VOC2012) Results, 2012. 6, 8
- [16] Kun Fu, Zhonghan Chang, Yue Zhang, and Xian Sun. Point-based estimator for arbitrary-oriented object detection in aerial images. *IEEE TGRS*, 59(5):4370–4387, 2020. 2
- [17] R Girshick. Fast r-cnn. In *CVPR*, pages 1440–1448, 2015. 5
- [18] Meng-Hao Guo, Chengrou Lu, Zheng-Ning Liu, Ming-Ming Cheng, and Shiyong Hu. Visual attention network. *Computational Visual Media*, 2022. 3, 1
- [19] Meng-Hao Guo, Cheng-Ze Lu, Qibin Hou, Zheng-Ning Liu, Ming-Ming Cheng, and Shi-Min Hu. SegNeXt: Rethinking convolutional attention design for semantic segmentation. In *NeurIPS*, 2022. 3, 4, 1
- [20] Zonghao Guo, Chang Liu, Xiaosong Zhang, Jianbin Jiao, Xiangyang Ji, and Qixiang Ye. Beyond bounding-box: Convex-hull feature adaptation for oriented and densely packed object detection. In *CVPR*, 2021. 7
- [21] Jiaming Han, Jian Ding, Jie Li, and Gui-Song Xia. Align deep features for oriented object detection. *IEEE TGRS*, 2020. 1, 2, 7, 4
- [22] Jiaming Han, Jian Ding, Nan Xue, and Gui-Song Xia. ReDet: A rotation-equivariant detector for aerial object detection. In *CVPR*, 2021. 7, 2
- [23] Kaiming He, Xiangyu Zhang, Shaoqing Ren, and Jian Sun. Deep residual learning for image recognition. In *CVPR*, 2016. 6, 4
- [24] Kaiming He, Georgia Gkioxari, Piotr Dollár, and Ross Girshick. Mask R-CNN. In *ICCV*, 2017. 7, 2
- [25] Liping Hou, Ke Lu, Jian Xue, and Yuqiu Li. Shape-adaptive selection and measurement for oriented object detection. In *AAAI*, 2022. 7
- [26] Liping Hou, Ke Lu, Xue Yang, Yuqiu Li, and Jian Xue. G-rep: Gaussian representation for arbitrary-oriented object detection. *Remote Sensing*, 15(3):757, 2023. 2
- [27] Qibin Hou, Daquan Zhou, and Jiashi Feng. Coordinate attention for efficient mobile network design. In *CVPR*, pages 13713–13722, 2021. 3
- [28] Qibin Hou, Cheng-Ze Lu, Ming-Ming Cheng, and Jiashi Feng. Conv2former: A simple transformer-style convnet for visual recognition. *IEEE TPAMI*, 2024. 3, 4
- [29] Zibo Hu, Kun Gao, Xiaodan Zhang, Junwei Wang, Hong Wang, Zhijia Yang, Chenrui Li, and Wei Li. Emo2-detr: Efficient-matching oriented object detection with transformers. *IEEE TGRS*, 2023. 7
- [30] Steven Lang, Fabrizio Ventola, and Kristian Kersting. DAFNe: A one-stage anchor-free deep model for oriented object detection. *CoRR*, 2021. 7
- [31] Wentong Li, Yijie Chen, Kaixuan Hu, and Jianke Zhu. Oriented reppoints for aerial object detection. In *CVPR*, pages 1829–1838, 2022. 1, 2, 8

- [32] Weijie Li, Wei Yang, Yuenan Hou, Li Liu, Yongxiang Liu, and Xiang Li. Saratr-x: Towards building a foundation model for sar target recognition. *arXiv preprint*, 2024. 1
- [33] Weijie Li, Wei Yang, Tianpeng Liu, Yuenan Hou, Yuxuan Li, Zhen Liu, Yongxiang Liu, and Li Liu. Predicting gradient is better: Exploring self-supervised learning for sar atr with a joint-embedding predictive architecture. *ISPRS Journal of Photogrammetry and Remote Sensing*, 218:326–338, 2024. 1
- [34] Yuxuan Li, Qibin Hou, Zhaohui Zheng, Ming-Ming Cheng, Jian Yang, and Xiang Li. Large selective kernel network for remote sensing object detection. In *ICCV*, 2023. 1, 2, 3, 4, 5, 6, 7, 8
- [35] Yuxuan Li, Xiang Li, Yimain Dai, Qibin Hou, Li Liu, Yongxiang Liu, Ming-Ming Cheng, and Jian Yang. Lsknet: A foundation lightweight backbone for remote sensing. *IJCV*, 2024. 3
- [36] Yuxuan Li, Xiang Li, Weijie Li, Qibin Hou, Li Liu, Ming-Ming Cheng, and Jian Yang. Sardet-100k: Towards open-source benchmark and toolkit for large-scale sar object detection. *NeurIPS*, 2024. 1
- [37] Tsung-Yi Lin, Priya Goyal, Ross Girshick, Kaiming He, and Piotr Dollár. Focal loss for dense object detection. In *ICCV*, 2017. 7, 8, 2
- [38] Shiwei Liu, Tianlong Chen, Xiaohan Chen, Xuxi Chen, Qiao Xiao, Boqian Wu, Mykola Pechenizkiy, Decebal Mocanu, and Zhangyang Wang. More convnets in the 2020s: Scaling up kernels beyond 51x51 using sparsity. *ArXiv*, 2022. 2, 3
- [39] Zikun Liu, Hongzhen Wang, Lubin Weng, and Yiping Yang. Ship rotated bounding box space for ship extraction from high-resolution optical satellite images with complex backgrounds. *TGRS Letters*, 2016. 5, 6, 1
- [40] Zikun Liu, Hongzhen Wang, Lubin Weng, and Yiping Yang. Ship rotated bounding box space for ship extraction from high-resolution optical satellite images with complex backgrounds. *IEEE TGRS*, 13(8):1074–1078, 2016. 2
- [41] Zhuang Liu, Hanzi Mao, Chao-Yuan Wu, Christoph Feichtenhofer, Trevor Darrell, and Saining Xie. A convnet for the 2020s. In *CVPR*, 2022. 1
- [42] Yang Long, Yiping Gong, Zhifeng Xiao, and Qing Liu. Accurate object localization in remote sensing images based on convolutional neural networks. *IEEE TGRS*, 55(5):2486–2498, 2017. 1
- [43] Ilya Loshchilov and Frank Hutter. Decoupled weight decay regularization. *ArXiv*, 2017. 5
- [44] Chengqi Lyu, Wenwei Zhang, Haiyan Huang, Yue Zhou, Yudong Wang, Yanyi Liu, Shilong Zhang, and Kai Chen. RTMDet: An empirical study of designing real-time object detectors. *CoRR*, 2022. 2, 7, 8
- [45] Jie Mei, Yi-Bo Zheng, and Ming-Ming Cheng. D2ANet: Difference-aware attention network for multi-level change detection from satellite imagery. *Computational Visual Media*, 2023. 1
- [46] Qi Ming, Zhiqiang Zhou, Lingjuan Miao, Hongwei Zhang, and Linhao Li. Dynamic anchor learning for arbitrary-oriented object detection. *CoRR*, 2020. 8
- [47] Qi Ming, Junjie Song, and Zhiqiang Zhou. Oriented feature alignment for fine-grained object recognition in high-resolution satellite imagery. *ArXiv*, 2021. 2
- [48] Qi Ming, Lingjuan Miao, Zhiqiang Zhou, Junjie Song, Yunpeng Dong, and Xue Yang. Task interleaving and orientation estimation for high-precision oriented object detection in aerial images. *ISPRS Journal of Photogrammetry and Remote Sensing*, 196:241–255, 2023. 8
- [49] Mohammed Bany Muhammad and Mohammed Yeasin. Eigen-CAM: Class activation map using principal components. *CoRR*, 2020. 7
- [50] Kemal Oksuz, Selim Kuzucu, Tom Joy, and Puneet K Dokania. Moca: Mixture of calibrated experts significantly improves object detection. *ArXiv*, 2023. 6, 7
- [51] Xingjia Pan, Yuqiang Ren, Kekai Sheng, Weiming Dong, Haolei Yuan, Xiaowei Guo, Chongyang Ma, and Changsheng Xu. Dynamic refinement network for oriented and densely packed object detection. In *CVPR*, 2020. 8
- [52] Yifan Pu, Yiru Wang, Zhuofan Xia, Yizeng Han, Yulin Wang, Weihao Gan, Zidong Wang, Shiji Song, and Gao Huang. Adaptive rotated convolution for rotated object detection. In *ICCV*, pages 6589–6600, 2023. 1, 2
- [53] Wen Qian, Xue Yang, Silong Peng, Junchi Yan, and Yue Guo. Learning modulated loss for rotated object detection. In *AAAI*, 2021. 2
- [54] Shaoqing Ren, Kaiming He, Ross Girshick, and Jian Sun. Faster R-CNN: Towards real-time object detection with region proposal networks. In *NeurIPS*, 2015. 2, 7, 8
- [55] Junjie Song, Lingjuan Miao, Qi Ming, Zhiqiang Zhou, and Yunpeng Dong. Fine-grained object detection in remote sensing images via adaptive label assignment and refined-balanced feature pyramid network. *IEEE Journal of Selected Topics in Applied Earth Observations and Remote Sensing*, 16:71–82, 2022. 2
- [56] Xian Sun, Peijin Wang, Wanxuan Lu, Zicong Zhu, Xiaonan Lu, Qibin He, Junxi Li, Xue Rong, Zhujun Yang, Hao Chang, et al. Ringmo: A remote sensing foundation model with masked image modeling. *IEEE TGRS*, 61:1–22, 2022. 2
- [57] Xian Sun, Peijin Wang, Zhiyuan Yan, Feng Xu, Ruiping Wang, Wenhui Diao, Jin Chen, Jihao Li, Yingchao Feng, Tao Xu, Martin Weinmann, Stefan Hinz, Cheng Wang, and Kun Fu. FAIR1M: A benchmark dataset for fine-grained object recognition in high-resolution remote sensing imagery. *ISPRS Journal of Photogrammetry and Remote Sensing*, 2022. 5, 6, 8, 1
- [58] Xian Sun, Yu Tian, Wanxuan Lu, Peijin Wang, Ruigang Niu, Hongfeng Yu, and Kun Fu. From single- to multi-modal remote sensing imagery interpretation: a survey and taxonomy. *Science China Information Sciences*, 2023. 1
- [59] Di Wang, Qiming Zhang, Yufei Xu, Jing Zhang, Bo Du, Dacheng Tao, and Liangpei Zhang. Advancing plain vision transformer towards remote sensing foundation model. *IEEE TGRS*, 2022. 7
- [60] Jinwang Wang, Jian Ding, Haowen Guo, Wensheng Cheng, Ting Pan, and Wen Yang. Mask obb: A semantic attention-based mask oriented bounding box representation for multi-

- category object detection in aerial images. *Remote Sensing*, 11(24):2930, 2019. 2
- [61] Jinwang Wang, Wen Yang, Heng-Chao Li, Haijian Zhang, and Gui-Song Xia. Learning center probability map for detecting objects in aerial images. *IEEE TGRS*, 2021. 7
- [62] Yue Wu, Yinpeng Chen, Lu Yuan, Zicheng Liu, Lijuan Wang, Hongzhi Li, and Yun Fu. Rethinking classification and localization for object detection. In *CVPR*, pages 10186–10195, 2020. 4, 5
- [63] Gui-Song Xia, Xiang Bai, Jian Ding, Zhen Zhu, Serge Belongie, Jiebo Luo, Mihai Datcu, Marcello Pelillo, and Liangpei Zhang. DOTA: A large-scale dataset for object detection in aerial images. In *CVPR*, 2018. 1, 2, 5, 6
- [64] Zikai Xiao, Guoye Yang, Xue Yang, Taijiang Mu, Junchi Yan, and Shimin Hu. Theoretically achieving continuous representation of oriented bounding boxes. In *CVPR*, pages 16912–16922, 2024. 1, 2, 7
- [65] Xingxing Xie, Gong Cheng, Jiabao Wang, Xiwen Yao, and Junwei Han. Oriented R-CNN for object detection. In *ICCV*, 2021. 1, 2, 3, 4, 5, 7, 8
- [66] Chang Xu, Jian Ding, Jinwang Wang, Wen Yang, Huai Yu, Lei Yu, and Gui-Song Xia. Dynamic coarse-to-fine learning for oriented tiny object detection. In *CVPR*, pages 7318–7328, 2023. 7, 8
- [67] Yongchao Xu, Mingtao Fu, Qimeng Wang, Yukang Wang, Kai Chen, Gui-Song Xia, and Xiang Bai. Gliding vertex on the horizontal bounding box for multi-oriented object detection. *IEEE TPAMI*, 2021. 1, 2, 7, 8
- [68] Xue Yang and Junchi Yan. Arbitrary-oriented object detection with circular smooth label. In *ECCV*, 2020. 1, 2, 7
- [69] Xue Yang, Qingqing Liu, Junchi Yan, and Ang Li. R3Det: Refined single-stage detector with feature refinement for rotating object. *CoRR*, 2019. 7, 2, 4
- [70] Xue Yang, Jirui Yang, Junchi Yan, Yue Zhang, Tengfei Zhang, Zhi Guo, Xian Sun, and Kun Fu. SCRDet: Towards more robust detection for small, cluttered and rotated objects. In *ICCV*, 2019. 2, 7
- [71] Xue Yang, Liping Hou, Yue Zhou, Wentao Wang, and Junchi Yan. Dense label encoding for boundary discontinuity free rotation detection. In *CVPR*, pages 15819–15829, 2021. 2
- [72] Xue Yang, Junchi Yan, Qi Ming, Wentao Wang, Xiaopeng Zhang, and Qi Tian. Rethinking rotated object detection with Gaussian Wasserstein distance loss. In *ICML*, 2021. 1, 2, 7, 8
- [73] Xue Yang, Xiaojiang Yang, Jirui Yang, Qi Ming, Wentao Wang, Qi Tian, and Junchi Yan. Learning high-precision bounding box for rotated object detection via Kullback-Leibler divergence. In *NeurIPS*, 2021. 1, 2, 7
- [74] Xue Yang, Yue Zhou, Gefan Zhang, Jirui Yang, Wentao Wang, Junchi Yan, Xiaopeng Zhang, and Qi Tian. The KFIOU loss for rotated object detection. In *ICLR*, 2022. 1, 2, 7
- [75] Jingru Yi, Pengxiang Wu, Bo Liu, Qiaoying Huang, Hui Qu, and Dimitris Metaxas. Oriented object detection in aerial images with box boundary-aware vectors. In *WACV*, pages 2150–2159, 2021. 2
- [76] Bowen Yin, Xuying Zhang, Zhongyu Li, Li Liu, Ming-Ming Cheng, and Qibin Hou. Dformer: Rethinking rgb-d representation learning for semantic segmentation. *ICLR*, 2024. 3
- [77] Hongtian Yu, Yunjie Tian, Qixiang Ye, and Yunfan Liu. Spatial transform decoupling for oriented object detection. In *AAAI*, pages 6782–6790, 2024. 5
- [78] Yi Yu and Feipeng Da. Phase-shifting coder: Predicting accurate orientation in oriented object detection. In *CVPR*, pages 13354–13363, 2023. 7
- [79] Syed Sahil Abbas Zaidi, Mohammad Samar Ansari, Asra Aslam, Nadia Kanwal, Mamoona Asghar, and Brian Lee. A survey of modern deep learning based object detection models. *Digital Signal Processing*, 2022. 1
- [80] Ying Zeng, Yushi Chen, Xue Yang, Qingyun Li, and Junchi Yan. Ars-detr: Aspect ratio-sensitive detection transformer for aerial oriented object detection. *IEEE TGRS*, 62:1–15, 2024. 8
- [81] Zhaohui Zheng, Rongguang Ye, Ping Wang, Dongwei Ren, Wangmeng Zuo, Qibin Hou, and Ming-Ming Cheng. Localization distillation for dense object detection. In *CVPR*, pages 9407–9416, 2022. 2
- [82] Zhaohui Zheng, Yuming Chen, Qibin Hou, Xiang Li, Ping Wang, and Ming-Ming Cheng. Zone evaluation: Revealing spatial bias in object detection. *IEEE TPAMI*, 2024. 7

Strip R-CNN: Large Strip Convolution for Remote Sensing Object Detection

Supplementary Material

6. Dataset details

DOTA-v1.0 [63] is a large-scale dataset for remote sensing detection which contains 2806 images, 188,282 instances, and 15 categories: Plane (PL), Baseball diamond (BD), Bridge (BR), Ground track field (GTF), Small vehicle (SV), Large vehicle (LV), Ship (SH), Tennis court (TC), Basketball court (BC), Storage tank (ST), Soccer-ball field (SBF), Roundabout (RA), Harbor (HA), Swimming pool (SP), and Helicopter (HC). Each image is of the size in the range from 800×800 to 20000×20000 pixels and contains objects exhibiting a wide variety of scales, orientations, and shapes. The proportions of the training set, validation set, and testing set in DOTA-v1.0 are 1/2, 1/6, and 1/3, respectively. For single scale training and testing, we first crop the image into 1024×1024 patches with an overlap of 200 following the previous methods [1, 34, 52], we use both the training set and validation set for training, and the testing set for test.

DOTA-v1.5 [63] is a more challenging dataset using the same images as DOTA-v1.0, but the extremely small instances (less than 10 pixels) are also annotated. In this version, a new category, "Container Crane" (CC), has been introduced, and the number of small instances has significantly increased, with a total of 403,318 instances across the dataset. The number of images and dataset splits remains unchanged from DOTA-v1.0.

FAIR1M-v1.0 [57] is a recently published remote sensing dataset that consists of 15,266 high-resolution images and more than 1 million instances. All objects in the FAIR1M dataset are annotated with respect to 5 categories and 37 sub-categories by oriented bounding boxes. Each image is of the size in the range from 1000×1000 to $10,000 \times 10,000$ pixels and contains objects exhibiting a wide variety of scales, orientations, and shapes. The number of images of the train set and testing set in FAIR1M-1.0 are 16,488 and 8,137, respectively. During training, we apply the same preprocessing methods as DOTA-v1.0 dataset, resulting in multi-scale training and testing sets.

HRSC2016 [39] is a remote sensing dataset for ship detection that contains 1061 aerial images whose size ranges from 300×300 and 1500×900 . All images are sourced from Google Earth, and the dataset is divided into training, validation, and test sets, with 436 images for training, 181 for validation, and 444 for testing.

DIOR-R [6] dataset extends the DIOR remote sensing dataset by providing oriented bounding box (OBB) annotations. It includes 23,463 images, each with a resolution of

Table 12. Comparisons with large-kernel-based methods on the DOTA-v1.0 [63] dataset. Params and FLOPs are computed for backbone only. The StripNet-S backbone is pretrained on ImageNet for 300 epochs.

Method	Pre.	#P ↓	FLOPs ↓	mAP (%)
VAN-B1 [18]	IN	13.4M	52.7G	81.15
SegNext [19]	IN	13.1M	45.0G	81.12
ConvNext V2-N [41]	IN	15.0M	51.2G	80.81
★ Strip R-CNN-S	IN	13.3M	52.3G	82.28

800×800 pixels, and a total of 192,518 annotations.

7. Implementation details

In this paper, we adopt the approach outlined in previous works [1, 34] to implement multi-scale training and testing across the DOTA, DOTAv1.5, and FAIR1M datasets. Specifically, we rescale each image to three different scales (0.5, 1.0, 1.5) and then crop them into 1024×1024 patches, with a 500-pixel overlap between adjacent patches. It is important to note that throughout both the pre-training and fine-tuning stages, we did not utilize Exponential Moving Average (EMA) techniques. As a result, the performance metrics reported for LSKNet in the main table are based on results obtained without EMA.

8. FAIR1M benchmark results

Fine-grained category result comparisons with state-of-the-art methods on the FAIR1M-v1.0 dataset are given in Tab. 13

9. DOTA-v1.5 benchmark results

Fine-grained category result comparisons with state-of-the-art methods on the DOTA-v1.5 dataset are given in Tab. 14

10. More results of the effectiveness of the strip head

More result comparisons of two different detectors before and after incorporating the strip head are shown in Tab. 16. The results is obtained on DOTA-v1.0 dataset with single-scale training and testing. As can be seen in Tab. 16, we compare the performance of two different detectors before and after incorporating the strip head. The results demonstrate that our strip head consistently improves the performance of other detectors, confirming its effectiveness and generalizability. For LSKNet [34], our method achieves a

Table 13. Comparisons With the SOTA Models on the FAIR1M-v1.0 Datasets. *The correspondence between C1-C34 and object categories in the table (in order). C1: Boeing 737, C2: Boeing 747, C3: Boeing 777, C4: Boeing 787, C5: C919, C6: A220, C7: A321, C8: A330, C9: A350, C10: ARJ21, C11: passenger ship, C12: motorboat, C13: fishing boat, C14: tugboat, C15: engineering ship, C16: liquid cargo ship, C17: dry cargo ship, C18: warship, C19: small car, C20: bus, C21: cargo truck, C22: dump truck, C23: van, C24: trailer, C25: tractor, C26: excavator, C27: truck tractor, C28: basketball court, C29: tennis court, C30: football field, C31: baseball field, C32: intersection, C33: roundabout, C34: bridge.*

Method	C1 C18	C2 C19	C3 C20	C4 C21	C5 C22	C6 C23	C7 C24	C8 C25	C9 C26	C10 C27	C11 C28	C12 C29	C13 C30	C14 C31	C15 C32	C16 C33	C17 C34	mAP (%)
Gliding Vertex [67]	35.43 13.56	47.88 66.23	15.67 23.43	48.32 46.78	0.01 36.56	40.11 53.78	39.31 14.32	16.54 16.39	16.56 16.92	0.01 28.91	9.12 48.41	23.34 80.31	1.23 53.46	15.67 66.93	15.43 59.41	15.32 16.25	25.43 10.39	29.92
RetinaNet [37]	38.46 15.37	55.36 65.2	24.57 22.42	51.84 44.17	0.81 35.57	40.5 52.44	41.06 19.17	18.02 1.28	19.94 17.03	1.7 28.98	9.57 50.58	22.54 81.09	1.33 52.5	16.37 66.76	19.11 60.13	14.26 17.41	24.7 12.58	30.67
Cascade-RCNN [2]	40.42 14.53	52.86 68.19	29.07 28.25	52.47 48.62	0 40.4	44.37 58	38.35 13.66	26.55 0.91	17.54 16.45	0 30.27	12.1 38.81	28.84 80.29	0.71 48.21	15.35 67.9	18.53 55.67	14.63 20.35	25.15 12.62	31.18
Faster-RCNN [54]	36.43 13.16	50.68 68.42	22.5 28.37	51.86 51.24	0.01 43.6	47.81 57.51	43.83 15.03	17.66 3.04	19.95 17.99	0.13 29.36	9.81 58.26	28.78 82.67	1.77 54.5	17.65 71.71	16.47 59.86	16.19 16.92	27.06 11.87	32.12
RoI Transformer [11]	39.58 12.97	73.56 68.8	18.32 37.41	56.43 53.96	0 45.68	47.67 58.39	49.91 16.22	27.64 5.13	31.79 22.17	0 46.71	14.31 54.84	28.07 80.35	1.03 56.68	14.32 69.07	15.97 58.44	18.04 18.58	26.02 31.81	35.29
OFA-Net [47]	43.20 35.42	87.58 69.62	23.58 33.67	57.78 44.69	30.71 49.23	54.31 71.61	67.83 13.45	73.65 6.06	73.56 17.36	29.25 5.35	9.90 49.20	68.15 83.75	11.70 61.29	30.37 88.77	11.83 57.97	26.80 24.68	38.68 35.82	43.73
O-RCNN [65]	38.65 34.27	84.96 70.88	20.05 45.01	55.57 48.98	25.55 52.45	48.58 70.19	68.75 14.50	71.18 4.42	74.43 19.81	32.85 7.51	20.46 56.30	67.63 80.41	11.13 68.13	32.89 89.06	16.22 57.92	26.45 21.87	39.03 30.11	44.30
CHODNet [55]	40.23 13.68	53.39 70.12	29.65 28.38	54.04 49.11	0.02 44.02	46.26 60.78	43.12 14.48	27.61 4.96	20.89 17.60	0.01 30.09	12.34 47.91	29.34 82.11	1.71 54.10	17.77 69.97	17.72 19.57	16.78 59.91	27.51 14.38	32.46
OBB-ISP [56]	43.97 34.30	88.77 61.16	38.97 34.10	58.29 50.04	50.88 52.31	54.09 56.24	65.14 15.99	59.19 7.43	65.94 17.03	35.00 37.14	19.78 54.99	56.77 81.43	26.84 53.56	26.31 87.66	21.41 54.25	44.97 24.20	47.39 35.46	45.91
LSKNet-S [34]	- -	- -	- -	- -	- -	- -	- -	- -	- -	- -	- -	- -	- -	- -	- -	- -	- -	47.87
Ours																		
*Strip R-CNN-S	42.17 39.56	89.07 76.14	21.52 49.44	55.24 55.37	23.03 60.55	50.97 76.18	73.58 20.32	72.96 8.12	78.29 25.96	40.81 7.23	20.78 58.94	71.52 86.59	16.12 72.73	42.86 89.43	17.70 62.89	28.55 25.57	40.11 40.58	48.26

Table 14. Comparison with SOTA methods on the DOTA-v1.5 dataset with single-scale training and testing.

Method	Pre.	PL	BD	BR	GTF	SV	LV	SH	TC	BC	ST	SBF	RA	HA	SP	HC	CC	mAP(%) [↑]
RetinaNet-O [37]	IN	71.43	77.64	42.12	64.65	44.53	56.79	73.31	90.84	76.02	59.96	46.95	69.24	59.65	64.52	48.06	0.83	59.16
FR-O [54]	IN	71.89	74.47	44.45	59.87	51.28	68.98	79.37	90.78	77.38	67.50	47.75	69.72	61.22	65.28	60.47	1.54	62.00
Mask R-CNN [24]	IN	76.84	73.51	49.90	57.80	51.31	71.34	79.75	90.46	74.21	66.07	46.21	70.61	63.07	64.46	57.81	9.42	62.67
HTC [4]	IN	77.80	73.67	51.40	63.99	51.54	73.31	80.31	90.48	75.12	67.34	48.51	70.63	64.84	64.48	55.87	5.15	63.40
ReDet [22]	IN	79.20	82.81	51.92	71.41	52.38	75.73	80.92	90.83	75.81	68.64	49.29	72.03	73.36	70.55	63.33	11.53	66.86
LSKNet-S [34]	IN	72.05	84.94	55.41	74.93	52.42	77.45	81.17	90.85	79.44	69.00	62.10	73.72	77.49	75.29	55.81	42.19	70.26
PKINet-S [1]	IN	80.31	85.00	55.61	74.38	52.41	76.85	88.38	90.87	79.04	68.78	67.47	72.45	76.24	74.53	64.07	37.13	71.47
*Strip R-CNN-S	IN	80.04	83.26	54.40	75.38	52.46	81.44	88.53	90.83	84.80	69.65	65.93	73.28	74.61	74.04	69.70	38.98	72.27

improvement of 0.56%. Similarly, Oriented R-CNN [65] also receives a 0.3% performance gain, further validating that our approach is compatible with a wide range of detectors and is able to reliably enhance detection performance.

11. The effectiveness of the StripNet backbone

To validate the generality and effectiveness of our proposed StripNet backbone, we conduct experiments using various remote sensing detection frameworks. These include two-stage frameworks such as O-RCNN [65] and

RoI Transformer [11], as well as one-stage frameworks like S²ANet [21] and R3Det [69]. Result comparisons of two different detectors before and after incorporating the StripNet-S are shown in Tab. 15. The results is obtained on DOTA-v1.0 dataset with multi-scale training and testing. As can be seen in Tab. 15, we compare the performance of two different detectors before and after incorporating the StripNet-S backbone. The results demonstrate that our StripNet-S backbone consistently improves the performance of other detectors, confirming its effectiveness

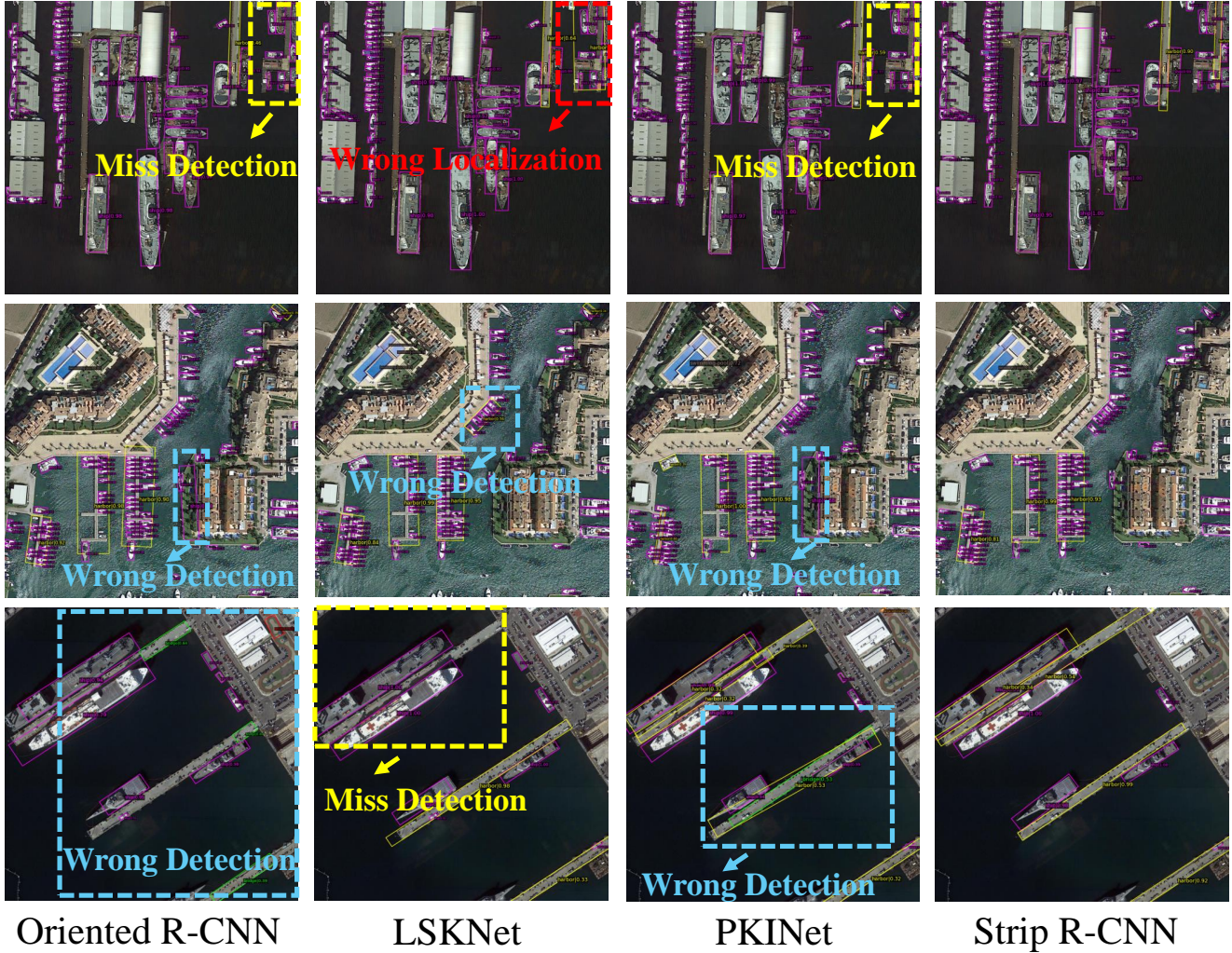


Figure 9. Detection results. Our method Strip R-CNN-S can successfully capture the high aspect ratio objects which validating the effectiveness of our approach.

and generalizability. For RoI Transformer [11], our method achieves a improvement of 7.11%. Similarly, Oriented R-CNN [65] also receives a 0.88% performance gain, S²ANet and R3Det obtains a improvement of 0.9% and 2.54% respectively, further validating that our approach is compatible with a wide range of detectors and is able to reliably enhance detection performance.

12. Comparisons with other large kernel networks

We also compare our Strip R-CNN-S with some popular high-performance backbone models which using large kernels in Tab. 12. In the three models under discussion, all have adopted large convolutional kernels. Specifically, VAN [18] utilizes dilated convolutions to expand the receptive field. While this technique effectively increases the

model’s receptive feild, it can also lead to the neglect of certain critical information, which is particularly disadvantageous for densely distributed objects in remote sensing scenes. SegNext [19] introduces a multi-branch large convolutional kernel structure, designed to capture richer feature information through multiple pathways. However, this architecture suffers from issues of feature confusion and feature redundancy, which may impact the model’s performance. Although these three methods validate the effectiveness of large convolutional kernels, they fail to adequately address the unique characteristics of data specific to remote sensing scenarios. This limitation restricts their generalization capabilities in such domains. In response to this challenge, our proposed method not only thoroughly analyzes the features of remote sensing data but also specifically optimizes for objects with high aspect ratios. Consequently,

Table 15. Effectiveness of StripNet-S backbone on other remote sensing object detection frameworks. The StripNet-S backbone is pre-trained on ImageNet [10] for 100 epochs.

Method	Backbone	PL	BD	BR	GTF	SV	LV	SH	TC	BC	ST	SBF	RA	HA	SP	HC	mAP (%)
RoI Trans. [11]	ResNet-50 [23]	88.65	82.60	52.53	70.87	77.93	76.67	86.87	90.71	83.83	82.51	53.95	67.61	74.67	68.75	61.03	74.61
	StripNet-S	89.10	85.45	63.61	82.84	80.95	85.84	88.68	90.84	88.35	87.92	72.12	71.37	79.73	83.32	75.77	81.72
O-RCNN [65]	ResNet-50 [23]	89.84	85.43	61.09	79.82	79.71	85.35	88.82	90.88	86.68	87.73	72.21	70.80	82.42	78.18	74.11	80.87
	StripNet-S	89.46	84.40	63.04	82.89	81.84	86.16	88.66	90.88	88.12	86.97	74.27	73.69	79.05	81.14	76.44	81.75
S ² ANet [21]	ResNet-50 [23]	88.89	83.60	57.74	81.95	79.94	83.19	89.11	90.78	84.87	87.81	70.30	68.25	78.30	77.01	69.58	79.42
	StripNet-S	89.31	84.94	61.01	81.87	81.34	85.10	88.69	90.76	86.89	87.49	67.94	68.74	77.96	78.82	73.90	80.32
R3Det [69]	ResNet-50 [23]	89.80	83.77	48.11	66.77	78.76	83.27	87.84	90.82	85.38	85.51	65.57	62.68	67.53	78.56	72.62	76.47
	StripNet-S	89.56	83.47	56.71	81.28	79.80	83.87	88.63	90.87	86.16	86.93	66.82	69.16	75.64	74.42	71.88	79.01

Table 16. Effectiveness of strip head on other remote sensing object detectors.

Method	Head	PL	BD	BR	GTF	SV	LV	SH	TC	BC	ST	SBF	RA	HA	SP	HC	mAP (%)
LSKNet-S [34]	Original Head	89.66	85.52	57.72	75.70	74.95	78.69	88.24	90.88	86.79	86.38	66.92	63.77	77.77	74.47	64.82	77.49
	Strip Head	89.71	83.50	56.18	78.86	79.83	84.66	88.16	90.86	88.30	86.11	67.02	66.27	76.19	71.79	63.39	78.05
O-RCNN [65]	Original Head	89.46	82.12	54.78	70.86	78.93	83.00	88.20	90.90	87.50	84.68	63.97	67.69	74.94	68.84	52.28	75.81
	Strip Head	89.48	82.33	53.95	72.83	78.60	77.97	88.12	90.89	85.84	84.76	64.42	67.55	74.57	70.31	60.05	76.11

our solution demonstrates superior performance in remote sensing applications, offering new insights and directions for addressing challenges in this field.

13. More detection results

We present additional detection results in Fig. 9. As can be seen in Fig. 9, previous methods, including Oriented R-CNN, LSKNet, and PKINet, frequently struggle with detecting high aspect ratio objects, often resulting in missed or incorrect detections. In contrast, our approach, Strip R-CNN, effectively detects these challenging objects.